



## Research Paper

Superiority of graphene over carbon analogs for enhanced photocatalytic H<sub>2</sub>-production activity of ZnIn<sub>2</sub>S<sub>4</sub>Yang Xia<sup>1</sup>, Qin Li<sup>\*,1</sup>, Kangle Lv, Dingguo Tang, Mei Li<sup>\*</sup>

Key Laboratory of Catalysis and Materials Science of the State Ethnic Affairs Commission &amp; Ministry of Education, South-Central University for Nationalities, Wuhan, 430074, PR China

## ARTICLE INFO

## Article history:

Received 16 November 2016  
 Received in revised form 20 January 2017  
 Accepted 22 January 2017  
 Available online 23 January 2017

**Keywords:**  
 Graphene  
 Carbon analogs  
 ZnIn<sub>2</sub>S<sub>4</sub>  
 Photocatalyst  
 Hydrogen production

## ABSTRACT

Graphene and its derivative reduced graphene oxide (RGO) have been widely considered to be a miracle modifier for most semiconductor photocatalysts over the past decade. However, the underlying advantage of graphene over its carbon analogs was rarely studied under the same experimental conditions to reveal its uniqueness. In this study, the promotion effect of RGO on ZnIn<sub>2</sub>S<sub>4</sub> (ZIS) semiconductor photocatalyst was systematically compared with that of carbon quantum dots (CQDs) and carbon nanotubes (CNTs). According to the property–photoactivity correlation analysis, the primary roles of these carbon analogs displayed an obvious dissimilarity. Among them, RGO manifested its superiority in enhancing the photoactivity of ZIS for hydrogen production from water splitting via controlling the morphology and boosting the charge carrier transferring. Our work revealed the exact contributions of different carbon materials to the promoted physicochemical properties and photocatalytic H<sub>2</sub>-production activity of ZIS semiconductor, and further affirmed the superiority of RGO over its carbon analogs in the construction of high-efficiency carbon–semiconductor based photocatalysts.

© 2017 Elsevier B.V. All rights reserved.

## 1. Introduction

Since the surprising and exciting discovery of graphene in 2004 [1], graphene and its derivative reduced graphene oxide (RGO) have aroused worldwide golden rush in photocatalysis fields due to its unique structural and electronic properties [2–7]. It has been universally accepted that graphene could serve as effective accelerant for most photocatalysts in various photocatalytic applications [8–15]. However, few reports focused on the systemic comparison of graphene to other carbon materials under the same experimental conditions, and there are also some voices of doubt to announce that graphene is not a miracle but just a promising material [16,17]. The primary role of graphene in the boost of photocatalytic performance of semiconductors is still mysterious.

As a well-known ternary chalcogenide semiconductor, ZnIn<sub>2</sub>S<sub>4</sub> (ZIS) with a narrow bandgap is a visible-light-driven, eco-friendly, and chemically stable photocatalyst for photocatalytic H<sub>2</sub> evolution [18–23]. More significantly, it is easy to fabricate ZIS with a nanosheet or nanosheet–self-assembly hierarchical microsphere structure, which allows it as a promising supporting matrix of

guest materials for the formation of heterostructured nanocomposites with enhanced photoactivity [20,24–27]. Similar to the situation of other frequently studied semiconductors, the photocatalytic performance of ZIS can also be enhanced with the help of RGO, which served as an electron–acceptor and transmitter [28,29]. For example, Li's group fabricated RGO/ZIS composite via a hydrothermal method and verified the promotion effect of RGO on the photocatalytic H<sub>2</sub>-production activity of ZIS [30]. And in the near few year, Peng's group [31] and Yu's group [24] reported in succession that carbon quantum dots (CQDs) and carbon nanotubes (CNTs) could also play a similar role as RGO. However, these carbon–semiconductor composite photocatalysts were studied separately under totally different experimental conditions. To the best of our knowledge, few researches were focused on the substantial effect of those carbon materials with different dimensionality on the physicochemical properties of ZIS semiconductor photocatalyst [16,32,33], and it remains a question whether graphene is the best choice among the carbon analogs for the enhancement of photocatalytic performance of ZIS semiconductor.

In this work, carbon materials with different dimensionality (including 0D CQDs, 1D CNTs, and 2D RGO) are combined with ZIS nanosheets under the same experimental condition. A systematic comparison was conducted to learn the exact contribution of different carbon materials to the enhanced photoactivity of ZIS semiconductor. It was found that RGO exhibited unique

\* Corresponding authors.

E-mail addresses: [liqin0518@mail.scuec.edu.cn](mailto:liqin0518@mail.scuec.edu.cn) (Q. Li), [ccnbl36@163.com](mailto:ccnbl36@163.com) (M. Li).<sup>1</sup> These authors contributed equally.

advantage among the studied carbon materials. The underlying reason was systematically investigated and finally proposed through series of characterizations. This work highlights the remarkable properties of graphene in the construction of high-efficiency carbon–semiconductor based composite photocatalysts.

## 2. Experimental section

### 2.1. Material preparations

All the reagents are analytical grade and used without further purifications. Multiwall CNTs (MWCNTs) (Shenzhen Nanotech Port Co., Ltd., China) were pretreated by refluxing in a mixture solution of 10 mL concentrated  $\text{HNO}_3$  (65–68%) and 30 mL concentrated  $\text{H}_2\text{SO}_4$  (95–98%) at 90 °C for 90 min [34,35]. CQDs were prepared by an electrochemical method according to Kang's work [36], using pure water as electrolyte and graphite rods (99.9%, Alfa Aesar Co. Ltd.) as both anode and cathode. The obtained CQDs exhibited typical PL upconversion property as shown in the supporting information (Fig. S1). They were able to be excited by long-wavelength light (from 450 to 900 nm) and emitted upconverted short-wavelength light (from 400 to 600 nm). It suggests that the CQDs could be acted as a powerful light harvesting and energy transfer component in the composite photocatalyst [36–39]. Graphene oxide (GO) was purchased from The Sixth Element Materials Technology Co., Ltd. in China and used without further treatment. The obtained three kinds of carbon material powders were redispersed into deionized water to be uniform suspensions with a concentration of 0.134 g/L.

Carbon nanomaterials decorated ZIS (C/ZIS) based on CQDs, CNTs, and RGO were synthesized via a facile microwave-assisted hydrothermal method under the same experimental conditions. Typically,  $\text{ZnCl}_2 \cdot 2\text{H}_2\text{O}$  (1 mmol),  $\text{InCl}_3 \cdot 4\text{H}_2\text{O}$  (2 mmol) and thioacetamide (TAA) (8 mmol) were mixed with 10 mL of carbon material aqueous dispersion, which has been proven by the pre-experiment to be the optimal volume for the enhanced photoactivity of the RGO/ZIS composites (see supporting information Fig. S2). The theoretical mass ratio of carbon material to ZIS was ca. 0.3 wt%. A certain amount of water and ethanol were added into the system to make the volume ratio of water/ethanol to be 2:1. The whole volume of the solution was maintained to be 27.2 mL. After magnetic stirring and ultrasonic treatment for 30 min, the homogeneous suspension was transferred into a 50 mL Teflon-lined autoclave, which was then placed in a microwave-hydrothermal synthesis system (MDS-6, Sineo, Shanghai, China) and maintained at 180 °C for 2 h. After the hydrothermal reaction, the precipitate was collected, washed with distilled water and ethanol until pH was 6~7, and then dried in a vacuum oven at 70 °C for 12 h. The prepared samples using CQDs, CNTs, and GO as precursors are named as CQDs/ZIS, CNTs/ZIS, and RGO/ZIS. It should be noted that the GO nanosheets were reduced to a certain extent to be RGO during the hydrothermal synthesis process, which has been proven by the comparison of the C 1 s XPS spectra of GO and the RGO/ZIS sample as shown in the supporting information (Fig. S3). Moreover, pure ZIS were prepared under the same conditions except that the carbon material aqueous dispersion was substituted by a corresponding volume of water and ethanol.

### 2.2. Characterization

Scanning electron microscopy (SEM) and Transmission electron microscopy (TEM) images were obtained to observe the morphology of the samples. The former was performed on an S-4800 Field Emission SEM (FESEM, Hitachi, Japan) at an accelerating voltage of 10 kV, while the latter was taken on a JEM-2100F electron microscope (JEOL, Japan) at 200 kV. Powder X-Ray diffraction (XRD)

patterns were obtained on an X-ray diffractometer (Rigaku, Japan) to determine the crystal phase of the prepared samples.  $\text{Cu K}\alpha$  ray ( $\lambda = 1.54056 \text{ \AA}$ ) was used as irradiation source and the scan rate was set to be  $0.05^\circ 2\theta \text{ s}^{-1}$ . The accelerating voltage and applied current were 40 kV and 80 mA, respectively. The average crystallite size was calculated using the Scherrer equation ( $d = 0.9\lambda/B \cos \theta$ , where  $d$ ,  $\lambda$ ,  $B$  and  $\theta$  are crystallite size,  $\text{Cu K}\alpha$  wavelength (0.154056 nm), full width at half maximum intensity (FWHM) in radians and Bragg's diffraction angle, respectively). X-ray photoelectron spectra (XPS) were performed on Multilab 2000 XPS system with a monochromatic  $\text{Mg K}\alpha$  source (excitation wavelength: 320 nm, scanning speed: 1200 nm/min, PMT voltage: 400 V, slit width: 10.0 nm). The C 1 s peak at 284.8 eV was set to be the reference of all the binding energies. The Brunauer–Emmett–Teller (BET) specific surface area ( $A_{\text{BET}}$ ) of the samples was analyzed by  $\text{N}_2$  adsorption in a Micromeritics ASAP 2020 nitrogen adsorption apparatus (USA). Prior to  $\text{N}_2$  adsorption measurements, all the samples were degassed at 180 °C. The  $A_{\text{BET}}$  was calculated from the adsorption data in the relative pressure ( $P/P_0$ ) range of 0.05–0.3 via a multipoint BET method. The corresponding pore size distribution (assuming a cylindrical pore model) was determined from the adsorption isotherm via the Barret–Joyner–Halender (BJH) method [40]. UV–vis diffused reflectance spectra (DRS) of the samples were obtained on a UV–vis spectrophotometer (UV2550, Shimadzu, Japan) using  $\text{BaSO}_4$  as the reflectance standard. Photoluminescence (PL) spectra were measured on a Fluorescence Spectrophotometer (F-7000, Hitachi, Japan) (excitation wavelength: 260 nm, scanning speed: 1200 nm  $\text{min}^{-1}$ , PMT voltage: 700 V, excitation and emission slit width: 5.0 nm).

### 2.3. Photoelectrochemical tests

Surface photovoltage (SPV) measurements were carried out using a lock-inbased SPS apparatus, which is constituted of a lock-in amplifier (SR830-DSP), a light chopper (SR540), a photovoltaic cell, and a computer. A 300W Xe lamp with a double-prism monochromator was used as the monochromatic light source. Mott–Schottky plots and transient photocurrent responses were measured on an electrochemical analyzer (CHI760e Instruments) in a standard three-electrode system using the prepared samples as the working electrodes, a Pt wire as the counter electrode,  $\text{Ag}/\text{AgCl}$  in saturated KCl as the reference electrode, and 0.4 M  $\text{Na}_2\text{SO}_4$  aqueous solution as the electrolyte. In the Mott–Schottky measurement, the working electrodes were prepared on a glassy carbon electrode, and the Mott–Schottky plots were obtained under direct current potential polarization at a fixed frequency of 80 Hz. The potential ranged from –0.8 to 0.4 V (vs  $\text{Ag}/\text{AgCl}$ ). In the transient photocurrent test, the working electrodes were prepared on an indium tin oxide (ITO) conductive glass according to Ye's work, using Nafion as adhesive [41]. A 420 nm-LED (3 W) (Shenzhen LAMPLIC Science Co. Ltd. China) was used as the visible-light source.

### 2.4. Photocatalytic hydrogen production

The photocatalytic  $\text{H}_2$  production experiments were performed in a 100 mL Pyrex three-neck flask at ambient temperature and atmospheric pressure [9]. In a typical photocatalytic  $\text{H}_2$ -production experiment, 50 mg of the prepared sample powders was suspended in 80 mL of triethanolamine aqueous solution (10 v%), and a certain amount of  $\text{H}_2\text{PtCl}_6 \cdot 6\text{H}_2\text{O}$  aqueous solution (10 g/L) was dripped into the suspension to deposit 0.3 wt% Pt onto the sample surface via a photochemical reduction method. Before the irradiation, the system was bubbled with  $\text{N}_2$  to completely remove the dissolved oxygen. The photocatalytic reaction was triggered by a 350 W Xenon arc lamp with a UV-cutoff filter ( $\geq 420 \text{ nm}$ ). Intermittently (one hour for example), a 0.4 mL of gas was sampled from

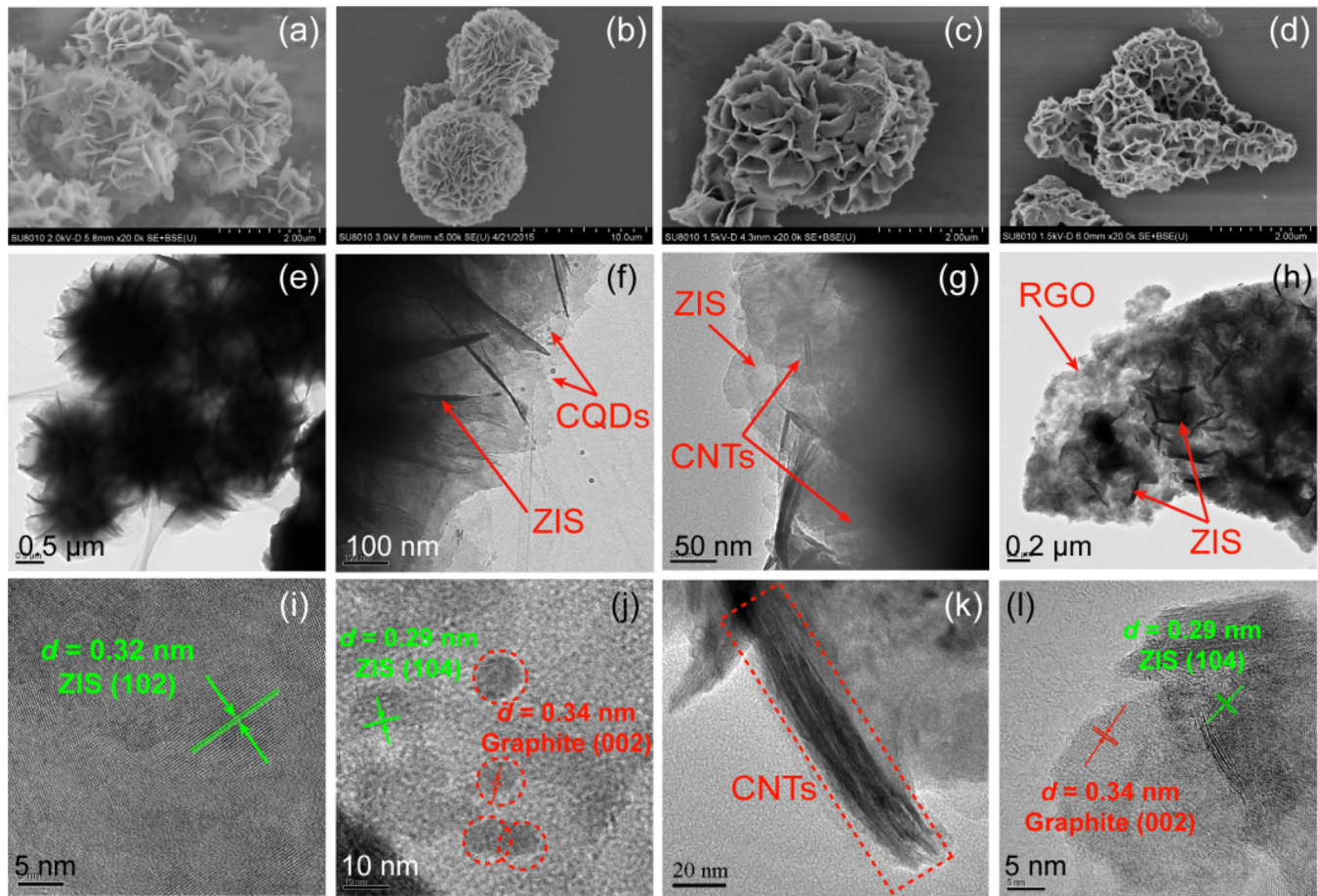


**Fig. 1.** (a–d) SEM, (e–h) TEM, and (i–l) high-resolution TEM images of the ZIS, CQDs/ZIS, CNTs/ZIS, and RGO/ZIS samples, respectively.

the flask, and H<sub>2</sub> content was analyzed by gas chromatography (GC2018, Shimadzu, Japan, TCD, with nitrogen as the carrier gas and 5 Å molecular sieve column).

The apparent quantum efficiency (QE) of the samples was calculated according to the following equation. The used irradiation source was four LEDs (420 nm, 3 W) (Shenzhen LAMPLIC Science Co. Ltd. China), which were positioned 1 cm away from the flask in four directions.

$$\text{QE} [\%] = \frac{\text{number of reacted electrons}}{\text{number of incident photons}} \times 100$$

$$= \frac{\text{number of evolved H}_2 \text{ molecules} \times 2}{\text{number of incident photons}} \times 100$$

### 3. Results and discussion

#### 3.1. Morphology

Scanning electron microscopy (SEM) and transmission electron microscopy (TEM) were carried out to observe the effect of carbon materials on the morphology of ZIS. Fig. 1 shows the representative SEM and TEM images of the prepared pure ZIS and C/ZIS composites. As can be seen, the pure ZIS is self-organized into a unique hierarchical peony-like spherical structure (Fig. 1a and e). With the introduction of CQDs and CNTs, the morphology of ZIS maintained nearly the same (Fig. 1b and c). Notably, there are not apparent CNTs or CQDs on the surface of the ZIS microspheres in the SEM images, while they could be clearly found in the corresponding TEM (Fig. 1f and g) and high-resolution TEM images (Fig. 1j and k). The pos-

sible reason will be explained later. Differently, RGO/ZIS displays a totally distinct sheet-on-sheet structure other than microsphere (Fig. 1d and h). The result indicates that the addition of different carbon materials has a distinct effect in regulating the morphology of the ZIS semiconductor. Particularly, RGO nanosheets played a unique role on the morphology control of ZIS other than CQDs and CNTs.

According to the above observation, the formation mechanism of ZIS in the presence of carbon materials with different dimensionality is proposed as shown in Fig. 2. Firstly, the Zn<sup>2+</sup> and In<sup>3+</sup> positive ions adhered onto negatively-charged surface of carbon materials by static electrical force [42]. Then, TAA slowly released S<sup>2-</sup> ions into the aqueous solution to react with Zn<sup>2+</sup> and In<sup>3+</sup> ions, thus the ZIS crystals were in situ formed on the surface of carbon materials and gradually grew up to be nanosheets due to the intrinsic lamellar structure of hexagonal-phased ZIS [30]. Among the studied carbon materials, CQDs and CNTs are low-dimension materials, those ZIS nanosheets covered the surface of them and were self-assembled into microsphere without any obstruction. In consequence, part of CNTs and CQDs must be wrapped in the ZIS microsphere, which explained the reason of the absence of CNTs and CQDs on the surface of ZIS microsphere in the SEM image (Fig. 1b and c). In the case of RGO/ZIS, the ZIS nanosheets firstly in situ grew on the RGO surface, similar to the cases of CNTs/ZIS and CQDs/ZIS. However, RGO owns a large size in two dimensions, so the further self-assembling process of ZIS nanosheets was prevented due to the steric hindrance. In consequence, the RGO/ZIS is formed as a sheet-on-sheet structure. According to the proposed formation mechanism, it is reasonable to estimate that more sur-

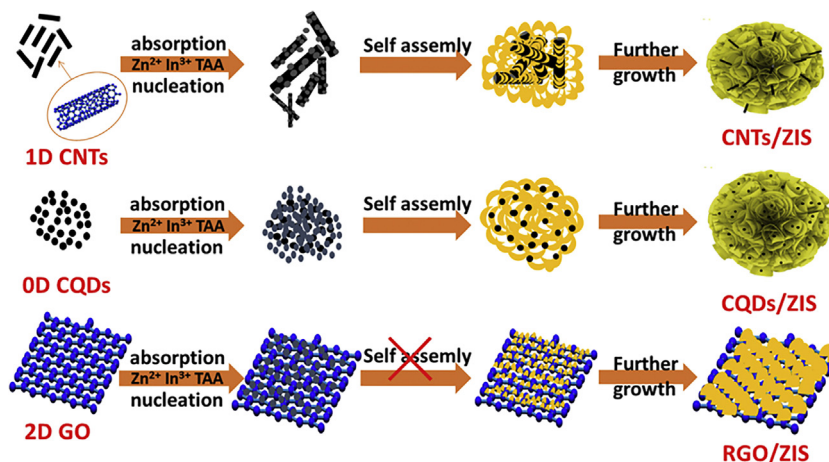


**Fig. 2.** Proposed mechanism for the formation of CNTs/ZIS, CQDs/ZIS, and RGO/ZIS nanocomposite with different morphologies.

**Table 1**

Physicochemical properties and photocatalytic H<sub>2</sub>-production activities of the ZIS, CQDs/ZIS, CNT/ZIS, and RGO/ZIS samples.

Sample	Crystallite size <sup>a</sup> [nm]	d (006) space <sup>b</sup> [Å]	A <sub>BET</sub> [m <sup>2</sup> g <sup>-1</sup> ]	H <sub>2</sub> -production rate [μmol h <sup>-1</sup> g <sup>-1</sup> ]	QE [%]
ZIS	9.7	4.16	80.7	625.6	1.1
CNTs/ZIS	9.9	4.16	54.0	1601.5	2.3
CQDs/ZIS	10.4	4.18	81.7	1767.7	2.3
RGO/ZIS	11.0	4.21	78.1	2640.8	4.4

<sup>a</sup> Average crystallite sizes of all the samples are determined by the broadening of hexagonal ZIS (102) facet diffraction peak using Scherrer formula.

<sup>b</sup> d space of (006) facet was calculated from  $2d \sin \theta / \lambda$ .

face of RGO would be exposed in the composite than that of CNTs and CQDs. Such difference resulted in many unique properties of RGO/ZIS, which will be discussed in detail later.

### 3.2. XRD and XPS analysis

Powder X-ray diffraction (XRD) was conducted to identify the effect of carbon materials on the crystallographic structure and crystallinity of ZIS. At a glance in Fig. 3a, the ZIS and C/ZIS samples display nearly the same diffraction peaks at 2θ values of 21.4, 27.7, 30.4, 39.8, 47.2, 52.4 and 55.7°, which can be indexed to (006), (102), (104), (108), (110), (116), and (022) facet crystal planes of hexagonal ZIS, respectively (JCPDS No. 65-2023) [43]. It seems that the presence of carbon nanomaterials has little influence on the crystallographic structure of ZIS in the composite [28]. However, a closer look at the XRD peak for (006) facet discovered a slight low-angle shift for the C/ZIS samples compared with the bare ZIS (Fig. 3b), and the corresponding data of d (006) spaces of the samples were listed in Table 1 [44]. The results showed that the introduction of carbon materials led to an increase of the d (006) space of ZIS, and RGO was the most obvious one, up to 0.05 Å. It is possibly caused by the tight interaction between ZIS crystals and carbon material, which gave a macro-residual tensile stress to the ZIS and caused the regional lattice expansion [45]. In this case, the interaction force between RGO and ZIS might be the strongest among the three C/ZIS composite samples.

There are no apparent XRD peaks observed for carbon materials, which may be due to the small amount and relatively low diffraction intensity of carbon material in the composite [9]. However, the XRD peak intensities of the C/ZIS samples were apparently enhanced than that of the ZIS sample. The calculated average crystallite sizes of ZIS crystals based on the hexagonal ZIS (102) facet are shown in Table 1, which follow an order of RGO/ZIS > CQDs/ZIS > CNTs/ZIS > ZIS. It demonstrates that RGO, CQDs, as well as CNTs could act as nucleation platform for ZIS crystals and thus promote the crystallization and growth of ZIS to a

certain extent, and RGO worked the best among the carbon materials. It was probably because of the more exposed surface of RGO in the composite, which supplied more nucleation sites for the ZIS crystals. The XRD result, from a side, confirmed the proposed formation mechanism of C/ZIS composite as discussed above.

Further evidence comes from the XPS analysis. As displayed in Fig. 4a–c, characteristic binding energies of 1022.0 and 1045.1 eV for Zn 2p, 445.0 and 452.5 eV for In 3d, and 162.0 eV for S 2p are observed over the bare ZIS sample. In comparison, the peaks of Zn 2p, In 3d, and S 2p in the C/ZIS samples shift toward lower binding energy by about 0.2–0.3 eV, similar to the reported result in other literatures [46]. It indicates a strong electronic interaction between carbon materials and ZIS in the composites, which is well consistent with the XRD result. Fig. 4d shows the comparison of C1 s XPS spectra of the CNT/ZIS, CQDs/ZIS, and RGO/ZIS samples. It can be seen that all the three C1 s spectra of the C/ZIS samples can be deconvoluted into three peaks at 284.8, 287.3 and 289.1 eV, which are assigned to the sp<sup>2</sup>-hybridized carbon (C=C), the C in C–O bonds, and the carboxylate C (O=C=O), respectively [47]. It means that there are some oxygen-containing groups such as hydroxyl and carboxyl groups on the surface of these carbon materials, which is favourable for their dispersion in the aqueous solution and participation in the photocatalytic H<sub>2</sub> production reaction [9].

### 3.3. N<sub>2</sub> adsorption-desorption isotherms

The effect of different carbon materials on the BET specific surface area (A<sub>BET</sub>) and porous structure of ZIS was investigated using adsorption-desorption measurements. Fig. 5 shows the nitrogen adsorption-desorption isotherms of pure ZIS and C/ZIS nanocomposites. All of them conformed to type IV according to the Brunauer-Deming-Deming-Teller (BDDT) classification, indicating the presence of mesopores (2–50 nm) in the samples [48–50]. The corresponding pore size distribution curves shown in the inset of Fig. 5 further confirmed the presence of mesopores. In addition, the hysteresis loops of all the samples show a high adsorption at a

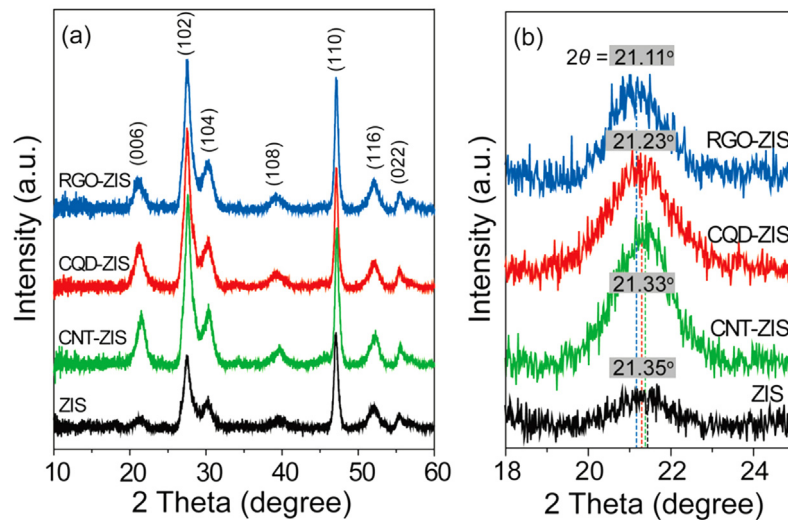


**Fig. 3.** (a) XRD patterns and (b) magnification of ZIS (006) facet diffraction peak shifts of the ZIS, CNT/ZIS, CQDs/ZIS, and RGO/ZIS samples.

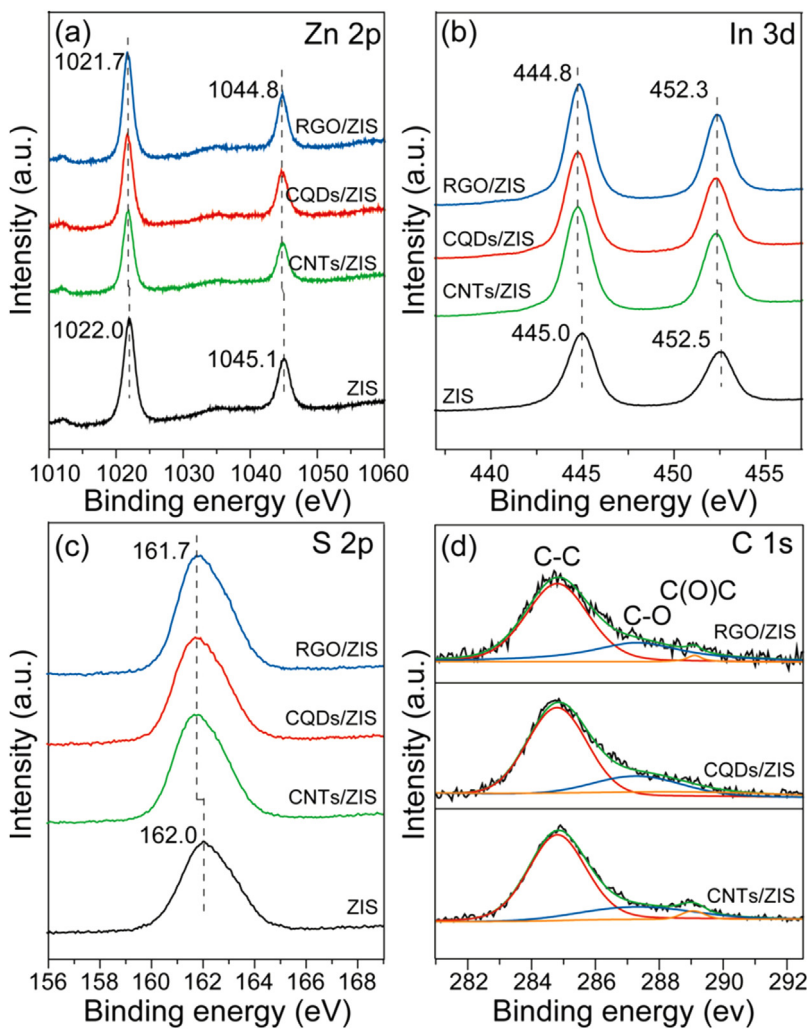


**Fig. 4.** XPS spectra of (a) Zn 2p, (b) In 3d, (c) S 2p, and (d) C 1s in the ZIS, CNT/ZIS, CQDs/ZIS, and RGO/ZIS samples.

high relative pressure ( $0.9 < P/P_0 < 1.0$ ), conforming to the shape of type H3. Such feature indicates that large slit-shaped macropores were formed between the plate-like petals [10]. This result is well-

consistent with the SEM image of the ZIS and C/ZIS nanocomposites, which shows that the obtained nanocomposites are consisting of nanosheets (Fig. 1). The surface area of the sample was determined

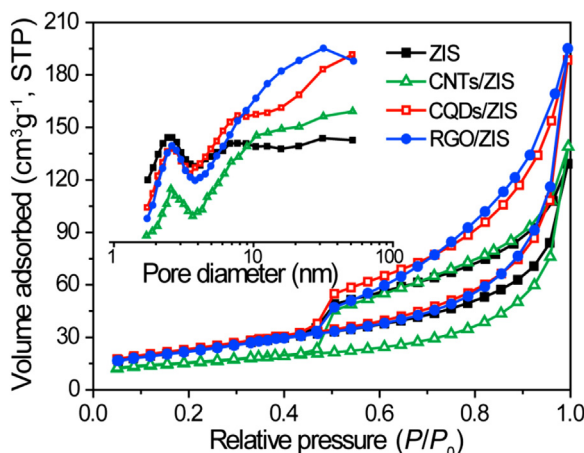


**Fig. 5.** Nitrogen adsorption–desorption isotherms and corresponding pore size distribution curves (inset) of pure ZIS and C/ZIS nanocomposites.

by a multipoint BET method using adsorption data in the relative pressure ( $P/P_0$ ) range of 0.05–0.3. The results were summarized in Table 1. It can be seen that the  $A_{\text{BET}}$  of CNTs/ZIS ( $54.0 \text{ m}^2 \text{ g}^{-1}$ ) and RGO/ZIS ( $78.1 \text{ m}^2 \text{ g}^{-1}$ ) are smaller than that of ZIS ( $80.7 \text{ m}^2 \text{ g}^{-1}$ ), which is due to the blockage of partial macropores between the ZIS nanosheets by the CNTs and RGO. Besides, it is worthy to note that the  $A_{\text{BET}}$  of RGO/ZIS is much higher than that of CNTs/ZIS. It can be attributed to the more uncovered surface as discovered in the electron microscopy results (Fig. 1). Differently, the presence of CQDs increases the  $A_{\text{BET}}$  of ZIS in a small degree ( $81.7 \text{ m}^2 \text{ g}^{-1}$ ), which is because the CQDs decorated on the ZIS petals increase the surface roughness. The  $N_2$  adsorption–desorption result further verifies the proposed mechanism of C/ZIS composites as discussed above.

#### 3.4. Optical and photoelectrochemical analysis

To investigate the effect of carbon materials on the electronic band structure of ZIS semiconductor, UV/Vis diffuse reflectance spectra (DRS) and Mott–Schottky plots were collected for the prepared ZIS, CNTs/ZIS, CQDs/ZIS, and RGO/ZIS samples. On one hand, DRS result shows that the addition of carbon materials did not significantly influence the band gap of ZIS semiconductor (Fig. 6a). All the samples exhibit an absorption edge at approximately 520 nm. According to the plots of the  $(\alpha h\nu)^2$  versus photon energy ( $h\nu$ ) (Kubelka–Munk function) for the ZIS semiconductor with a direct bandgap [51,52], the bandgap energy of the samples were estimated to be 2.64 eV (Fig. 6b). However, the light absorbance of ZIS was apparently enhanced after the introduction of carbon materials in the visible–light region from 500 to 800 nm. Such enhancement is attributed to the adsorption of black–color carbon nanomaterials

in the interior or on the surface of ZIS [53]. The corresponding color change was shown in the inset of Fig. 6a. Further observation indicated that the absorbance capacity of CNTs/ZIS and CQDs/ZIS was almost the same, while the RGO/ZIS sample exhibited a little bit higher absorption than others. It might be attributed to the larger exposed surface of RGO, which absorbed more visible light. The DRS result is also in accordance with the above proposed formation mechanism.

On the other hand, Mott–Schottky plots show that the conduction band edge ( $E_{\text{CB}}$ ) potential of ZIS semiconductor was apparently affected by the introduction of carbon materials. Fig. 7a displays that all the linear plots possess positive slopes, indicating the typical n-type characteristic of the C/ZIS materials. Therefore, the derived flat-band potentials according to the x intercepts of the linear region could be approximately considered as the  $E_{\text{CB}}$  potentials. For the bare ZIS, the  $E_{\text{CB}}$  potential was about  $-0.79 \text{ V}$  vs. Ag/AgCl at pH 5.45. With the addition of carbon materials, it was positive-shifted to be  $-0.59$ ,  $-0.57$ , and  $-0.55 \text{ V}$  for CNTs/ZIS, CQDs/ZIS and RGO/ZIS composites, respectively. Similar results were reported in other literatures [28,54,55]. Such anodic shift was probably due to the high electrical conductivity and low overpotential of carbon materials during the electrochemical test [56,57]. More significantly, the interaction between carbon material and ZIS contributed to the shift of the fermi level and thus resulted in the change of the  $E_{\text{CB}}$  potential.

It should be noted that, although the  $E_{\text{CB}}$  potential of C/ZIS composite was more positive than that of ZIS, it still thermodynamically enables the photocatalytic  $H_2$  production ( $H^+/\text{H}_2$ :  $-0.52 \text{ V}$  vs. Ag/AgCl at pH 5.45 according to the equation  $V_{\text{Ag/AgCl}} = V_{\text{NHE}} - 0.197 - 0.059 \text{ pH}$ ) [56,58]. Combined with the bandgap energy obtained by the DRS result (Fig. 6b), the band structures of the samples were schematically illustrated in Fig. 7b.

The photoluminescence (PL) spectra of the prepared samples were investigated to disclose the trapping, separation and transfer behaviors of charge carriers, because PL emission results from the electron–hole recombination [26]. As shown in Fig. 8a, the PL intensity of the samples follows an order of RGO/ZIS < CQDs/ZIS < CNTs/ZIS < ZIS. It demonstrated that the samples containing carbon materials possessed a lower recombination rate of electrons and holes than the bare ZIS, and that of the RGO/ZIS sample was the lowest one. It was because the carbon materials with high electroconductivity could capture the photogenerated electrons from the ZIS surface, boosting the separation and transfer efficiency of electron–hole pairs. Obviously, RGO played a much better role than other two carbon materials during the capturing process.

To further verify the effect of carbon materials on the charge transfer efficiency of ZIS, we conducted the surface photovoltage (SPV) spectra and transient photocurrent responses of C/ZIS samples. The results were shown in Fig. 8b and c, respectively. In Fig. 8b,

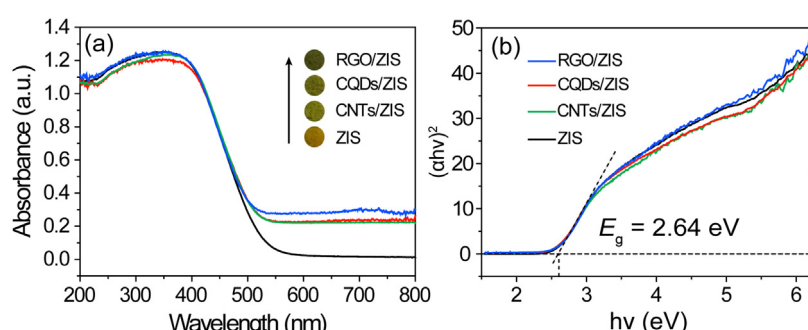


**Fig. 6.** (a) UV-vis diffuse reflectance spectra and (b) plot of transformed Kubelka–Munk function versus the energy of the light absorbed over the CNTs/ZIS, CQDs/ZIS and RGO/ZIS samples.

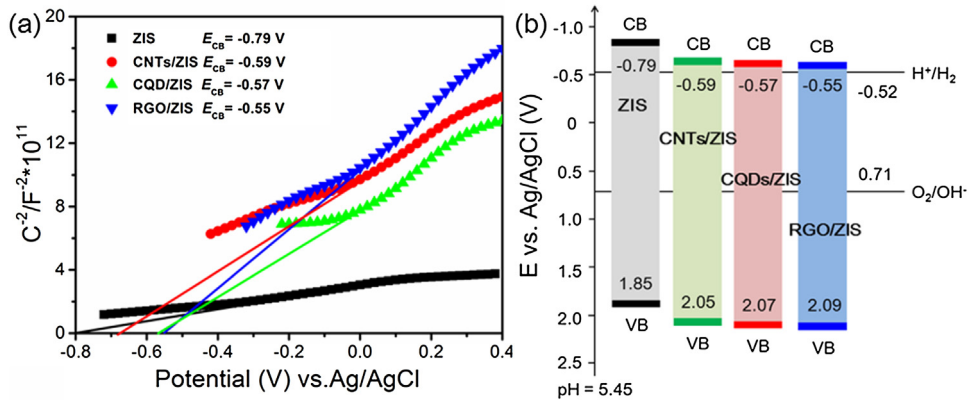


**Fig. 7.** (a) Mott–Schottky plots of the ZIS, CNTs/ZIS, CQDs/ZIS and RGO/ZIS samples at fixed frequency of 80 Hz in 0.4 M  $Na_2SO_4$  ( $pH = 5.45$ ). (b) Schematic illustration of band structures (CB: conduction band, VB: valence band) of the ZIS, CNTs/ZIS, CQDs/ZIS and RGO/ZIS samples vs. Ag/AgCl at  $pH = 5.45$ .

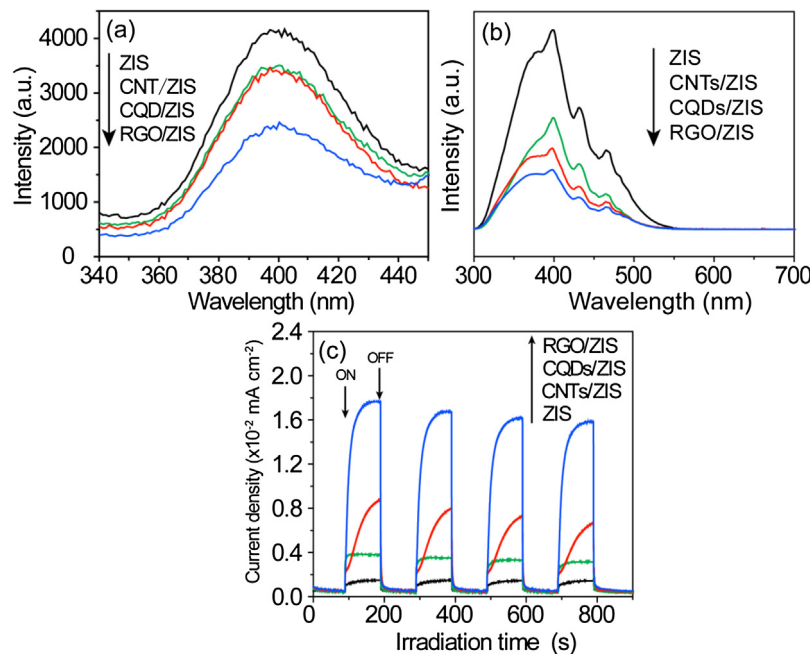


**Fig. 8.** (a) Comparison of PL spectra of the prepared samples. The excitation wavelength was 260 nm. (b) Comparison of the SPV spectra of the ZIS, CNTs/ZIS, CQDs/ZIS and RGO/ZIS samples. (c) Transient photocurrent responses of the prepared samples in 0.4 M  $Na_2SO_4$  aqueous solution.

all the samples displayed an obvious SPV response ranging from 300 to 550 nm, with a main SPV peak at about 400 nm. Notably, the SPV response edge of ZIS was similar to its band edge as shown in the DRS result (Fig. 6a). It implicates that the SPV signal of ZIS semiconductor was mainly attributed to the band–band electronic transition [3]. With the introduction of carbon material, the SPV response of the C/ZIS composite was weakened apparently than that of bare ZIS. It is because the carbon materials loaded over the ZIS surface easily captured the photogenerated electrons and lessened the amount of the electrons on the ZIS, which retarded the horizon transfer of photogenerated electrons [59]. The SPV intensities of the samples followed an order of RGO/ZIS < CQDs/ZIS < CNTs/ZIS < ZIS, which exhibited the same change law with the PL spectra (Fig. 8a). It is not surprising because the participant surface area of carbon material in the CNTs/ZIS and CQDs/ZIS composites for electron transfer was apparently smaller than that in RGO/ZIS as discussed before (Fig. 2). In consequence, the decreased degree of PL and SPV intensities over RGO/ZIS were larger than those of CQDs and CNTs-loaded ZIS because more electrons on the ZIS surface were captured by RGO. Considering that the photocatalysis

reactions always happen on the surface of photocatalyst, it is reasonable to assume that the RGO/ZIS composite would provide much more electrons to participate in the photocatalysis reaction.

As expected, the transient photocurrent responses provide a direct evidence for the higher charge transfer efficiency and higher electron concentration across RGO and ZIS interfaces (Fig. 8c). Under visible–light irradiation (at 420 nm), it is clear that the incorporation of carbon nanomaterials significantly promoted the photocurrent response of ZIS semiconductor, verifying the intimate interfacial contacts between carbon and ZIS semiconductor [60]. In addition, it can be observed that the current density of RGO/ZIS stood out in the crowd among the C/ZIS samples, further indicating that RGO provided best platform for the electron transport. The phenomenon is totally–consistent with the PL (Fig. 8a) and SPV spectra (Fig. 8b).

### 3.5. Photocatalytic performance

To confirm the assumption as discussed above, the photocatalytic  $H_2$ –production performance of the prepared samples

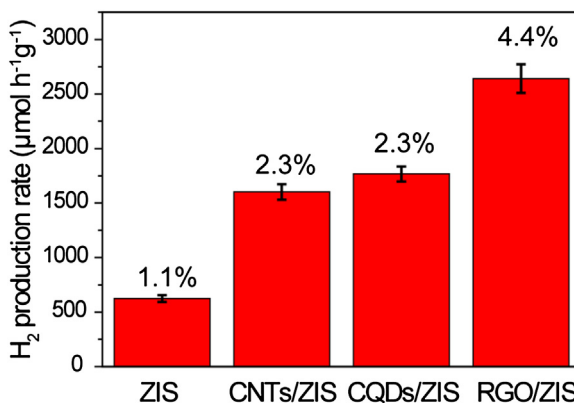


**Fig. 9.** Comparison of  $H_2$ -production rates over the ZIS, CNTs/ZIS, CQDs/ZIS and RGO/ZIS samples.

was evaluated under visible-light irradiation. The triethanolamine aqueous solution (10 v%) was used as sacrificial reagent and Pt (0.3 wt% to the sample powders) as cocatalyst. Fig. 9 and Table 1 show the photocatalytic  $H_2$ -production rates of the obtained samples. Typically, the  $H_2$  production rates of the samples ZIS, CNTs/ZIS, CQDs/ZIS, and RGO/ZIS were 625.6, 1601.5, 1767.7, and 2640.8  $\mu\text{mol g}^{-1} \text{h}^{-1}$ , respectively. The corresponding QE at 420 nm were 1.1, 2.3, 2.3, and 4.4%, respectively. It was found that the introduction of carbon materials apparently contributed to the enhanced photocatalytic performance of pure ZIS. The enhancing effect of carbon material on the ZIS semiconductor followed an order of RGO > CQDs > CNTs. It is worthy to note that such order is fully consistent with XRD, DRS, PL, SPV, and transient photocurrent results as displayed above. So, we can come to a deduction that crystallinity, light harvest, and electron transfer efficiency are main influence factors on the photoactivity of ZIS. More importantly, it can be also inferreded that the kind of carbon materials did have significant influence on these physicochemical properties of ZIS semiconductor. In detail, the morphology of ZIS semiconductor was determined by the dimensionality of carbon materials. Low-dimension carbon materials (0D CQDs and 1D CNTs) resulted in a flower-like microsphere structure, while high-dimension carbon materials (2D RGO) led to a sheet-on-sheet structure. In the latter case, RGO has more surfaces exposed to the external, which provided more nucleation sites, higher visible-light absorption ability, more adsorption sites, and larger space for the charge-carrier transfer. The resulted higher crystallinity, light harvest capacity, specific surface area and surface electron concentration were all beneficial to the enhanced photocatalytic  $H_2$  production reaction. Therefore, 2D RGO contributed to a highest enhancement factor for the photocatalytic  $H_2$  production efficiency over ZIS semiconductor, followed with 0D CQDs and 1D CNTs.

#### 4. Conclusions

In this study, the superior effect of RGO on the physicochemical properties and photocatalytic activity of ZIS semiconductor was highlighted by the comparison with its carbon analogs CQDs and CNTs under the same experimental conditions. Other than low-dimensional CQDs and CNTs, the unique 2D structure of RGO gave rise to a steric hindrance and inhibited the self-assembling process of ZIS nanosheets into microspheres. Therefore, RGO would not be wrapped into the microsphere and be able to expose more surface area than CQDs and CNTs in the composites. Such important difference afforded the RGO/ZIS sample improved crystallinity, enhanced light harvest capacity, enlarged specific surface area, increased surface electron concentration and finally boosted photo-

catalytic  $H_2$  production efficiency than other samples. Interestingly, all the change discipline of the studied properties of the samples followed a same order of RGO/ZIS, CQDs/ZIS, CNTs/ZIS, and ZIS. Using 0.3 wt% Pt as cocatalyst and 10 v% triethanolamine aqueous solution as sacrificial reagent, the obtained  $H_2$ -production rate of the RGO/ZIS sample was 1.5, 1.6, and 4.2 times higher than that of the CQDs/ZIS, CNTs/ZIS and ZIS samples, respectively. This work not only highlights the intrinsical role of carbon materials in the enhanced photocatalytic performance of ZIS semiconductor for  $H_2$  production, but also provides significant guidance to take full advantage of predominant properties of graphene in designing more efficient photocatalysts.

#### Acknowledgements

This work was supported by National Natural Science Foundation of China (21503281, 21571192), Fundamental Research Funds for the Central Universities (CZQ15008), and Project of Wuhan Science and Technology (2015070504020220), and Natural Science Foundation of South-Central University for Nationalities (YZZ14001, XTZ15016).

#### Appendix A. Supplementary data

Supplementary data associated with this article can be found, in the online version, at <http://dx.doi.org/10.1016/j.apcatb.2017.01.060>.

#### References

- [1] K.S. Novoselov, A.K. Geim, S.V. Morozov, D. Jiang, Y. Zhang, S.V. Dubonos, I.V. Grigorieva, A.A. Firsov, *Science* 306 (2004) 666–669.
- [2] N. Zhang, M.Q. Yang, S.Q. Liu, Y.G. Sun, Y.J. Xu, *Chem. Rev.* 115 (2015) 10307–10377.
- [3] Q. Li, X. Li, S. Wageh, A. Al-Ghamdi, J.G. Yu, *Adv. Energy Mater.* 5 (2015) 1500010.
- [4] Q.J. Xiang, B. Cheng, J.G. Yu, *Angew. Chem. Int. Ed.* 54 (2015) 11350–11366.
- [5] L.K. Putri, W.J. Ong, W.S. Chang, S.P. Chai, *Appl. Surf. Sci.* 358 (2015) 2–14.
- [6] X. Li, J.G. Yu, S. Wageh, A.A. Al-Ghamdi, J. Xie, *Small* 48 (2016) 6640–6696.
- [7] L.J. Fang, X.L. Wang, Y.H. Li, P.F. Liu, Y.L. Wang, H.D. Zeng, H.G. Yang, *Appl. Catal. B: Environ.* 200 (2017) 578–584.
- [8] X.K. Zeng, Z.Y. Wang, N. Meng, D.T. McCarthy, A. Deletic, J.H. Pan, X.W. Zhang, *Appl. Catal. B: Environ.* 202 (2017) 33–41.
- [9] Q. Li, B.D. Guo, J.G. Yu, J.R. Ran, B.H. Zhang, H.J. Yan, J.R. Gong, *J. Am. Chem. Soc.* 133 (2011) 10878–10884.
- [10] Q.J. Xiang, J.G. Yu, M. Jaroniec, *J. Am. Chem. Soc.* 134 (2012) 6575–6578.
- [11] Z.G. Mou, Y.J. Wu, J.H. Sun, P. Yang, Y.K. Du, C. Lu, *ACS Appl. Mater. Interfaces* 6 (2014) 13798–13806.
- [12] J.J. Ding, W.H. Yan, S. Sun, J. Bao, C. Gao, *ACS Appl. Mater. Interfaces* 6 (2014) 12877–12884.
- [13] K. Iwashina, A. Iwase, Y.H. Ng, R. Amal, A. Kudo, *J. Am. Chem. Soc.* 137 (2015) 604–607.
- [14] J.X. Low, J.G. Yu, W.K. Ho, *J. Phys. Chem. Lett.* 6 (2015) 4244–4251.
- [15] N. Zhang, M.Q. Yang, Z.R. Tang, Y.J. Xu, *ACS Nano* 8 (2013) 623–633.
- [16] N. Zhang, Y.H. Zhang, M.Q. Yang, Z.R. Tang, Y.J. Xu, *J. Catal.* 299 (2013) 210–221.
- [17] S.W. Cao, J.G. Yu, *J. Photochem. Photobiol. C* 27 (2016) 72–99.
- [18] S.H. Shen, L. Zhao, L.J. Guo, *Mater. Res. Bull.* 44 (2009) 100–105.
- [19] B. Chai, T.Y. Peng, P. Zeng, X.H. Zhang, X.J. Liu, *J. Phys. Chem. C* 115 (2011) 6149–6155.
- [20] L. Wei, Y.J. Chen, J.L. Zhao, Z.H. Li, *Beilstein J. Nanotechnol.* 4 (2013) 949–955.
- [21] K. Batabyal, S.E. Lu, J.J. Vittal, *Cryst. Growth Des.* 16 (2016) 2231–2238.
- [22] X. Li, J.G. Yu, M. Jaroniec, *Chem. Soc. Rev.* 45 (2016) 2603–2636.
- [23] W. Yang, L. Zhang, J.F. Xie, X.D. Zhang, Q.H. Liu, T. Yao, S.Q. Wei, Q. Zhang, Y. Xie, *Angew. Chem. Int. Ed.* 55 (2016) 6716–6720.
- [24] Q. Li, C. Cui, H. Meng, J.G. Yu, *Chem. Asian J.* 9 (2014) 1766–1770.
- [25] Y.J. Chen, R.K. Huang, D.Q. Chen, Y.S. Wang, W.J. Liu, X.N. Li, Z.H. Li, *ACS Appl. Mater. Interfaces* 4 (2012) 2273–2279.
- [26] Z.Y. Zhang, K.C. Liu, Z.Q. Feng, Y.N. Bao, B. Dong, *Sci. Rep.* 6 (2016) 19221.
- [27] Y. Xia, Q. Li, K.L. Lv, M. Li, *Appl. Surf. Sci.* 398 (2017) 81–88.
- [28] J.Y. Chen, H.M. Zhang, P.R. Liu, Y.B. Li, X.L. Liu, G.Y. Li, P.K. Wong, T.C. An, H.J. Zhao, *Appl. Catal. B: Environ.* 168 (2015) 266–273.
- [29] L. Yuan, M.Q. Yang, Y.J. Xu, *J. Mater. Chem. A* 2 (2014) 14401–14412.
- [30] L. Ye, J.L. Fu, Z. Xu, R.S. Yuan, Z.H. Li, *ACS Appl. Mater. Interfaces* 6 (2014) 3483–3490.
- [31] B. Chai, T.Y. Peng, P. Zeng, X.H. Zhang, *Dalton Trans.* 41 (2012) 1179–1186.

- [32] Y.T. Liang, B.K. Vijayan, O. Lyandres, K.A. Gray, M.C. Hersam, *J. Phys. Chem. Lett.* 3 (2012) 1760–1765.
- [33] P. Pathak, L.H. Israel, E.J.M. Pereira, V.R. Subramanian, *ACS Appl. Mater. Interfaces* 8 (2016) 13400–13409.
- [34] H.X. Shi, J.Y. Chen, G.Y. Li, X. Nie, H.J. Zhao, P.K. Wong, T.C. An, *ACS Appl. Mater. Interfaces* 5 (2013) 6959–6967.
- [35] Y. Xia, Q. Li, X.F. Wu, K.L. Lv, D.G. Tang, M. Li, *Appl. Surf. Sci.* 391 (2017) 565–571.
- [36] H. Ming, Z. Ma, Y. Liu, K.M. Pan, H. Yu, F. Wang, Z.H. Kang, *Dalton Trans.* 41 (2012) 9526–9531.
- [37] P. Chen, F.L. Wang, Z.F. Chen, Q.X. Zhang, Y.H. Su, L.Z. Shen, K. Yao, Y. Liu, Z.W. Cai, W.Y. Lv, G.G. Liu, *Appl. Catal. B: Environ.* 204 (2017) 250–259.
- [38] F.F. Duo, Y.W. Wang, C.M. Fan, X.C. Zhang, Y.F. Wang, *J. Alloys Compd.* 685 (2016) 34–41.
- [39] H. Zhang, L.X. Zhao, F.L. Geng, L.H. Guo, B. Wan, Y. Yang, *Appl. Catal. B: Environ.* 180 (2016) 656–662.
- [40] J.G. Yu, Q. Li, S.W. Liu, M. Jaroniec, *Chem. Eur. J.* 19 (2013) 2433–2441.
- [41] G.G. Liu, G.X. Zhao, W. Zhou, Y.Y. Liu, H. Pang, H.B. Zhang, D. Hao, X.G. Meng, P. Li, T. Kako, J.H. Ye, *Adv. Funct. Mater.* 26 (2016) 6822–6829.
- [42] Q. Li, H. Meng, J.G. Yu, W. Xiao, Y.Q. Zheng, J. Wang, *Chem. Eur. J.* 20 (2014) 1176–1185.
- [43] L. Ye, Z.H. Li, *Appl. Catal. B: Environ.* 160–161 (2014) 552–557.
- [44] F. Tian, R.S. Zhu, J. Zhong, P. Wang, F. Ouyang, G. Cao, *Int. J. Hydrogen Energy* 41 (2016) 20156–20171.
- [45] B.C. Qiu, Y. Zhou, Y.F. Ma, X.L. Yang, W.Q. Sheng, M.Y. Xing, J.L. Zhang, *Sci. Rep.* 5 (2015) 8591.
- [46] L. Ye, J.L. Fu, Z. Xu, R.S. Yuan, Z.H. Li, *ACS Appl. Mater. Interfaces* 6 (2014) 3483–3490.
- [47] H.W. Tien, Y.L. Huang, S.Y. Yang, J.Y. Wang, C.C.M. Ma, *Carbon* 49 (2011) 1550–1560.
- [48] K.S.W. Sing, D.H. Everett, R.A.W. Haul, L. Moscou, R.A. Peirotti, J. Rouquerol, T. Siemieniewska, *Pure Appl. Chem.* 57 (1985) 603–619.
- [49] H. Yang, K.L. Lv, J.J. Zhu, Q. Li, D.G. Tang, W.K. Ho, M. Li, S.A.C. Carabineiro, *Appl. Surf. Sci.* 401 (2017) 333–340.
- [50] Q. Li, H. Meng, P. Zhou, Y.Q. Zheng, J. Wang, J.G. Yu, J.R. Gong, *ACS Catal.* 3 (2013) 882–889.
- [51] H.T. Yu, X. Quan, Y.B. Zhang, N. Ma, S. Chen, H.M. Zhao, *Langmuir* 24 (2008) 7599–7604.
- [52] G. Wang, G. Chen, Y.G. Yu, X. Zhou, Y.J. Teng, *RSC Adv.* 3 (2013) 18579–18586.
- [53] S. Stankovich, D.A. Dikin, R.D. Piner, K.A. Kohlhaas, A. Kleinhammes, Y.Y. Jia, Y. Wu, S.T. Nguyen, R.S. Ruoff, *Carbon* 45 (2007) 1558–1565.
- [54] L.W. Zhang, H.B. Fu, Y.F. Zhu, *Adv. Funct. Mater.* 18 (2008) 2180–2189.
- [55] Y.B. Li, H.M. Zhang, P.R. Liu, D. Wang, Y. Li, H.J. Zhao, *Small* 9 (2013) 3336–3344.
- [56] S.B. Yang, Y.J. Gong, J.S. Zhang, L. Zhan, L.L. Ma, Z.Y. Fang, R. Vajtai, X.C. Wang, P.M. Ajayan, *Adv. Mater.* 25 (2013) 2452–2456.
- [57] Y.G. Li, H.L. Wang, L.M. Xie, Y.Y. Liang, G.S. Hong, H.J. Dai, *J. Am. Chem. Soc.* 133 (2011) 7296–7299.
- [58] J.S. Zhang, X.F. Chen, K. Takanabe, K. Maeda, K. Domen, J.D. Epping, X.Z. Fu, M. Antonietti, X.C. Wang, *Angew. Chem. Int. Ed.* 49 (2010) 441–444.
- [59] L.J. Zhang, R. Zheng, S. Li, B.K. Liu, D.J. Wang, L.L. Wang, T.F. Xie, *ACS Appl. Mater. Interfaces* 6 (2014) 13406–13412.
- [60] Z.X. Chen, Y. Wu, J.J. Xu, F.X. Wang, J. Wang, J.Y. Zhang, Z.Y. Ren, Y.H. He, G.C. Xiao, *J. Mol. Catal. A: Chem.* 401 (2015) 66–72.